Table 1 Very Large Array observations of the pulsar-powered nebula G5.27–0.90

	Epoch 1	Epoch 2
Date observed	1993 Feb. 02	1999 Oct. 23
Array configuration	BnA	BnA
On-source integratin time (h)	3.3	2.8
Centre frequency (GHz)	8.44	8.46
Bandwidth (MHz)	75	100

These observations were used for proper motion measurements. Both observations used the same pointing centre, namely (J2000) right ascension (RA) 18 h 01 min 00.035 s, declination (Dec) – 24° 51′ 27.260″. Absolute flux densities were determined using observations of the source 3C286, while antenna gains were calibrated using observations every 15–20 min of the extragalactic source PMN J1751–2524, displaced 2.1° from G5.27–0.90. The resulting images were formed using natural weighting and multi-frequency synthesis with 100-mas pixels, deconvolved using a maximum entropy algorithm, and then smoothed with a circular gaussian of FWHM 0.90″.

the range predicted above. The low braking index of the Vela pulsar[20], discrepant pulsar–SNR ages in other pulsar–SNR associations[23,24], and the fact that many pulsars with small characteristic ages have no associated SNR (refs 2 and 3), all suggest that PSR B1757–24 is not a statistical anomaly. If other pulsars are indeed older than they seem, our understanding of pulsar velocities, asymmetries in supernova explosions, the fraction of supernovae that produce pulsars, and the physics of neutron star structure and cooling must all be reconsidered[12,25–27]. □

Received 14 March; accepted 25 May 2000.

1. Manchester, R. N. & Taylor, J. H. *Pulsars* (Freeman, San Francisco, 1977).
2. Braun, R., Goss, W. M. & Lyne, A. G. Three fields containing young pulsars: The observable lifetime of supernova remnants. *Astrophys. J.* **340,** 355–361 (1989).
3. Stappers, B. W., Gaensler, B. M. & Johnston, S. A deep search for pulsar wind nebulae using pulsar grating. *Mon. Not. R. Astron. Soc.* **308,** 609–617 (1999).
4. Manchester, R. N., D'Amico, N. & Tuohy, I. R. A search for short period pulsars. *Mon. Not. R. Astron. Soc.* **212,** 975–986 (1985).
5. Manchester, R. N., Kaspi, V. M., Johnston, S., Lyne, A. G. & D'Amico, N. A remarkable pulsar-supernova remnant association. *Mon. Not. R. Astron. Soc.* **253,** 7P–10P (1991).
6. Frail, D. A. & Kulkarni, S. R. Unusual interaction of the high-velocity pulsar PSR 1757–24 with the supernova remnant G5.4–1.2. *Nature* **352,** 785–787 (1991).
7. Shull, J. M., Fesen, R. A. & Saken, J. M. Pulsar reenergization of old supernova remnant shells. *Astrophys. J.* **346,** 860–868 (1989).
8. Frail, D. A., Kassim, N. E. & Weiler, K. W. Radio imaging of two supernova remnants containing pulsars. *Astron. J.* **107,** 1120–1127 (1994).
9. Becker, R. H. & Helfand, D. J. A new class of nonthermal radio sources. *Nature* **313,** 115–118 (1985).
10. Caswell, J. L. *et al.* The Galactic radio sources G5.4–1.2 and G5.27–0.90. *Mon. Not. R. Astron. Soc.* **225,** 329–334 (1987).
11. Lyne, A. G. & Lorimer, D. R. High birth velocities of radio pulsars. *Nature* **369,** 127–129 (1994).
12. Cordes, J. M. & Chernoff, D. F. Neutron star population dynamics. II. Three-dimensional space velocities of young pulsars. *Astrophys. J.* **505,** 315–338 (1998).
13. van Buren, D. & McCray, R. Bow shocks and bubbles are seen around hot stars by IRAS. *Astrophys. J.* **329,** L93–L96 (1988).
14. Frail, D. A. & Scharringhausen, B. R. A radio survey for pulsar wind nebulae. *Astrophys. J.* **480,** 364–370 (1997).
15. Thompson, D. J. *et al.* EGRET high-energy gamma-ray pulsar studies. I. Young spin-powered pulsars. *Astrophys. J.* **436,** 229–238 (1994).
16. Gaensler, B. M. & Johnston, S. The pulsar/supernova remnant connection. *Mon. Not. R. Astron. Soc.* **277,** 1243–1253 (1995).
17. Cioffi, D. F., McKee, C. F. & Bertschinger, E. Dynamics of radiative supernova remnants. *Astrophys. J.* **334,** 252–265 (1988).
18. Lyne, A. G., Pritchard, R. S. & Smith, F. G. Crab pulsar timing 1982–1987. *Mon. Not. R. Astron. Soc.* **233,** 667–676 (1988).
19. Kaspi, V. M., Manchester, R. N., Siegman, B., Johnson, S. & Lyne, A. G. On the spin-down of PSR B1509–58. *Astrophys. J.* **422,** L83–L86 (1994).
20. Lyne, A. G., Pritchard, R. S., Graham-Smith, F. & Camilo, F. Very low braking index for the Vela pulsar. *Nature* **381,** 497–498 (1996).
21. Lyne, A. G. *et al.* A giant glitch in PSR B1757–24. *Mon. Not. R. Astron. Soc.* **281,** L14–L16 (1996).
22. Blandford, R. D., Applegate, J. H. & Hernquist, L. Thermal origin of neutron star magnetic fields. *Mon. Not. R. Astron. Soc.* **204,** 1025–1048 (1983).
23. Blandford, R. D. & Romani, R. W. On the interpretation of pulsar braking indices. *Mon. Not. R. Astron. Soc.* **234,** 57P–60P (1988).
24. Seward, F. D., Harnden, F. R. Jr, Murdin, P. & Clark, D. H. MSH 15-52: A supernova remnant containing two compact X-ray sources. *Astrophys. J.* **267,** 698–710 (1983).
25. Frail, D. A., Goss, W. M. & Whiteoak, J. B. Z. The radio lifetime of supernova remnants and the distribution of pulsar velocities at birth. *Astrophys. J.* **437,** 781–793 (1994).
26. Brazier, K. T. S. & Johnston, S. The implications of radio-quiet neutron stars. *Mon. Not. R. Astron. Soc.* **305,** 671–679 (1999).
27. Umeda, H., Shibazaki, N., Nomoto, K. & Tsuruta, S. Thermal evolution of neutron stars with internal frictional heating. *Astrophys. J.* **408,** 186–193 (1993).
28. Sault, R. J. & Killeen, N. E. B. *The Miriad User's Guide* (Australia Telescope National Facility, Sydney, 1998); also at ⟨http://www.atnf.csiro.au/computing/software/miriad⟩.
29. Keys, R. G. Cubic convolution interpolation for digital image processing. *IEEE Trans. Acoustic Speech Signal Process* **29,** 1151–1160 (1981).
30. Powell, M. J. D. A method for minimizing a sum of squares of non-linear functions without calculating derivatives. *Comput. J.* **7,** 303–307 (1964).

Acknowledgements

We thank V. Kaspi and D. Chakrabarty for useful discussions, N. Kassim for supplying 90-cm data on G5.4–1.2 and A. Lyne for providing timing data on PSR B1757–24. The National Radio Astronomy Observatory is a facility of the National Science Foundation operated under cooperative agreement by Associated Universities, Inc. B.M.G. acknowledges the support of NASA through a Hubble Fellowship awarded by the Space Telescope Science Institute.

Correspondence and requests for materials should be addressed to B.M.G. (e-mail: bmg@space.mit.edu).

Realignment of the flux-line lattice by a change in the symmetry of superconductivity in UPt_3

Andrew Huxley*, Pierre Rodière*, Donald M^{c}K. Paul†, Niels van Dijk‡, Robert Cubitt§ & Jacques Flouquet*

* *CEA, Département de Recherche Fondamentale sur la Matière Condensée, SPSMS, 38054 Grenoble Cedex 9, France*
† *University of Warwick, Department of Physics, Coventry CV4 7AL, UK*
‡ *Delft University of Technology, Mekelweg 15, 2629 JB Delft, The Netherlands*
§ *Institut Laue Langevin, BP156, 38042 Grenoble Cedex 9, France*

In 1957, Abrikosov[1] described how quanta of magnetic flux enter the interior of a bulk type II superconductor. It was subsequently predicted that, in an isotropic superconductor, the repulsive forces between the flux lines would cause them to order in two dimensions, forming a hexagonal lattice[2]. Flux-line lattices with different geometry can also be found in conventional (type II) superconductors[3]; however, the ideal hexagonal lattice structure should always occur when the magnetic field is applied along a hexagonal crystal direction[4]. Here we report measurements of the orientation of the flux-line lattice in the heavy-fermion superconductor[5] UPt_3, for this special case. As the temperature is increased, the hexagonal lattice, which is initially aligned along the crystal symmetry directions, realigns itself with the anisotropic superconducting gap. The superconductivity in UPt_3 is unusual (even compared to unconventional oxide superconductors[6]) because the superconducting gap has a lower rotational symmetry than the crystal structure. This special feature enables our data to demonstrate clearly the link between the microscopic symmetry of the superconductivity and the mesoscopic physics of the flux-line lattice. Moreover, our observations provide a stringent test of the theoretical description of the unconventional superconductivity in UPt_3.

In a recent study[7] of the magnetic borocarbide $TmNi_2B_2C$ it was shown that a flux-line lattice (FLL) can align itself with a coexisting modulated magnetic structure. Here we present evidence that a FLL can also be aligned to the intrinsic symmetry of the superconducting order. In previous work on UPt_3, the FLL geometry was measured at low temperature as a function of field for magnetic fields directed parallel to a crystallographic **a** direction[8,9]. The symmetry and orientation of the FLL for this field direction was found to be independent of the field strength, but a strong evolution of the distortion of the FLL geometry with field was observed. This has been interpreted to support a description of the superconductivity in terms of a two-component order parameter[10]. In the present

study we report a fundamental change in the symmetry of the FLL with temperature, when the field is applied parallel to the hexagonal **c** direction. Owing to the special choice of the hexagonal direction, the observed symmetry change cannot be explained by Fermi-surface anisotropy[11,12], which can otherwise provide a conventional explanation for the occurrence of different symmetry FLLs. The presence of this competing mechanism has complicated the interpretation of a previous study of the unconventional superconductor Sr_2RuO_4 (ref. 13).

Our measurements were performed on an annealed cylindrical single crystal, grown parallel to a crystallographic **a** direction by the Czochralski technique under ultrahigh vacuum. Conventional neutron diffraction detected no crystal mosaicity within an instrumental resolution of 0.35° (full-width at half-maximum), and the crystal's superconducting properties were measured to be similar to other high-quality samples[14,15].

The FLL was studied by small-angle neutron scattering with the D22 instrument at the Institut Laue Langevin, France. The neutron wavelength used was $\lambda_n = 8$ Å, which is above the Bragg cut-off for diffraction from the crystalline lattice. The applied magnetic field was initially aligned with the incident neutron beam and parallel to the crystal's hexagonal **c** axis. Neutrons, scattered via the interaction of their magnetic moments with spatial modulations of the magnetic field, were detected on a small-angle camera positioned 17.65 m from the sample. The sum of detected images for several small inclinations ('rocking angles') of the sample and field from the incident beam direction is simply related to the Fourier transform of the magnetic field distribution in the interior of the crystal. After subtraction of background scattering observed in the normal state, the summed image thus has the approximate geometry of the real FLL unit cell rotated through 90° about the field direction. But because only rocking angles about the vertical axis were explored, diffraction spots that lie almost directly above or below the incident beam are absent from the images in our study.

A schematic of the low-temperature phase diagram of UPt_3 is shown in Fig. 1. The distinctive feature of the phase diagram is the existence of three separate superconducting phases[16], labelled A, B and C. The Abrikosov mixed state occurs down to very low fields, H_{c1} (not shown), of only a few thousandths of a tesla. To explain the phase diagram and other experimental results, theoretical models have attributed different symmetries to the three phases[17,18] in accordance with group theory. The gap symmetries for one of the most successful theoretical descriptions[19](denoted E_{2u}) are shown in Fig. 1. In this model, the anisotropy of the superconducting gap in the basal plane for the A and C phases is predicted to be larger than

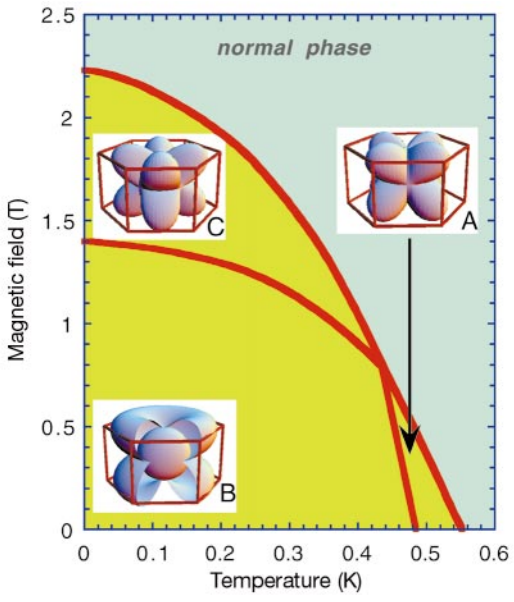

Figure 1 The low-temperature phase diagram of UPt_3 for magnetic fields parallel to the hexagonal crystal axis. Second-order phase transitions separate three different superconducting phases, labelled A, B and C. The values of the superconducting critical temperature and the critical field (at low fields) shown are the actual values measured for the crystal used in the present experiment. The geometric shapes show schematically the theoretical superconducting gap symmetries in the three phases for the E_{2u} theoretical model[19]. The gap magnitude is represented as the difference between the outer surfaces and inner spheres as a function of angle (a segment of the outer surface has been removed to show the inner sphere in the shape for the B phase). The frames define the hexagonal crystal symmetry. The assignment of the two shapes to the A and C phases was interchangeable depending on the sign of a coupling constant in the theoretical model: however, our experiment determines the assignment to be as shown.

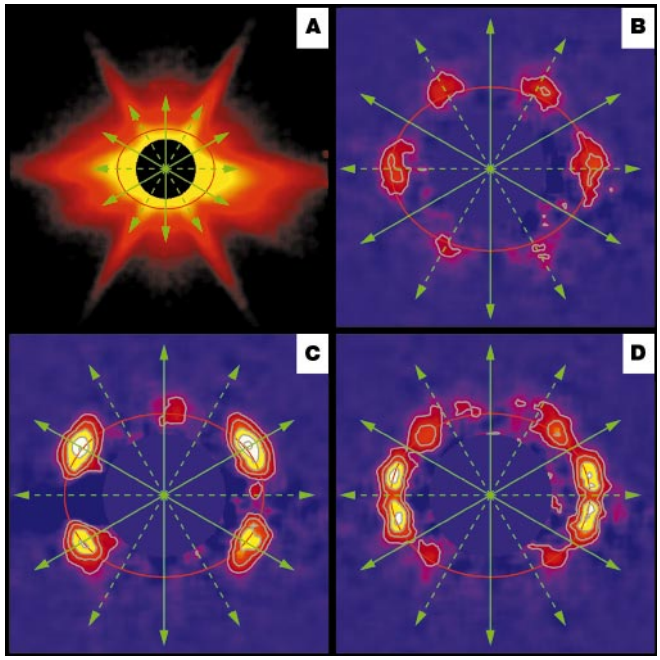

Figure 2 The measured small-angle neutron scattering from the flux-line lattice in UPt_3. **A**, the scattering seen on the small-angle neutron camera with the sample in the normal state at 600 mK; the data are shown on a logarithmic intensity scale. The solid lines show the crystallographic **a** directions and the dashed lines the **a*** directions, in the plane of the detector. The incident beam passes through the centre of the image, which is masked off. The ridges of scattered intensity parallel to crystallographic **a*** directions extending towards the edges of the image have an intrinsic metallurgical origin. The subsequent panels show the extra scattering in the superconducting state at 0.19 T relative to the normal-state background. Each image is an equal combination of measurements at two rocking angles of the sample and field (–0.25°and +0.25° about the vertical axis). The contours are spaced in equal steps of 100 counts per pixel per hour (the detector is divided into pixels of 0.75 cm). The fact that the rocking angles differ slightly from the optimum value to illuminate each individual spot means that the centre of gravity of each diffracted spot is slightly displaced from its ideal position. Furthermore, the diffraction condition to illuminate spots lying almost vertically above or below the incident beam is not satisfied. The ellipses indicate the approximate radial positions expected for diffraction spots from an ideal hexagonal lattice with $B = 0.19$ T (a mean wavevector transfer of 0.0065 $Å^{-1}$) at these rocking angles. The images all represent measurements made at low temperature (100–150 mK), but differ with respect to the field history before the measurement. Panel **B** shows the extra scattering after cooling the sample in a constant field from above T_c. Panel **C** shows the scattering after the sample was cooled in zero field, with the field applied subsequently at low temperature and then oscillated by 0.02 T about its final value. Panel **D** shows the scattering after the sample was cooled in zero field to $T_0 = 475$ mK (in the superconducting A phase). The field was applied and oscillated at T_0 and the sample was subsequently cooled to low temperature in a constant field.

for the B phase. The effects of both the Fermi surface anisotropy and the gap anisotropy on the orientation and symmetry of the FLL arise from non-local corrections[11] to the simple London model[20] description of the mixed state. In constant magnetic field, the non-local correction for a fixed Fermi surface anisotropy decreases only slightly (by a factor of 2) between zero temperature and the critical temperature, T_c. It acts to stabilize a hexagonal FLL aligned to the mirror planes of the hexagonal point group (along either the crystallographic **a** or **a*** directions). The expected increase in the anisotropy of the superconducting gap with temperature close to the B–A phase line could however lead to an increasing non-local correction with a four-fold symmetry, which might be sufficient to give a measurable deviation from a perfect hexagonal FLL. The motivation for our experiment was therefore to look for possible deviations from the ideal hexagonal FLL as the A phase was approached, and additionally to test for several more exotic flux-line structures that can in theory occur in unconventional superconductors[21,22].

Scattering from the FLL was found to depend on the field history in the superconducting state (Fig. 2). A hexagonal FLL was always formed when the sample was cooled in a constant field from above T_c (a field-cooled history denoted as 'FC'), with nearest-neighbour flux lines along **a** directions (Fig. 2B). The rocking width over which the diffraction spots were illuminated was measured to be rather broad (a full-width at half-maximum of 0.44°), a characteristic of a deformed FLL. The FC lattice is nucleated at the same time as the superconductivity, and is therefore sensitive to slight variations in T_c close to any defects. This gives a natural mechanism to align the FLL to the extended metallurgical structure shown in Fig. 2A. Figure 2C shows the scattering when the field was increased from zero at the measurement temperature, and then oscillated by 0.02 T about its final value (a field-oscillated history denoted as 'FO'). The nearest-neighbour directions between the flux lines now corresponds to **a*** directions. The rocking width was measured to be equal to the divergence of the incident neutron beam (a full-width at half-maximum of 0.14°), which is consistent with a highly ordered FLL. The same lattice orientation was in fact obtained for all field histories in which the applied magnetic field was varied significantly at low temperature, irrespective of any previous history. However, to be systematic in what follows, the crystal was always cooled from above T_c in zero field to the temperature at which the FO procedure was applied (the full procedure is then denoted as 'ZFC+FO'). An improvement in the degree of order of the FLL following a displacement of the flux lines, as observed here, has been reported for several conventional superconductors[23]. When the pinning is not too strong, displacing the flux lines allows the lattice to relax from a frozen metastable state distorted by pinning, to approach the arrangement most energetically favoured in the absence of pinning.

Because we are interested in the equilibrium structure, we will now focus our discussion on the measurements following the ZFC+FO process, and discuss the evolution of the FLL when this process was applied at different temperatures and the FLL measured directly at these temperatures. The integrated reflected intensity for a Bragg reflection from a sample of thickness t is given by

$$R(\mathbf{q}) = \frac{\gamma^2}{16\phi_0^2}\frac{\lambda_0^3 t}{\sin(2\theta)}\frac{|f(\mathbf{q})|^2}{S_0^2} \qquad (1)$$

where θ is the Bragg angle, S_0 is the unit cell area of the FLL, $\gamma = 1.91$ (the gyromagnetic ratio of the neutron), and ϕ_o is the flux quantum. The form factor $f(\mathbf{q})$ is the Fourier component of the magnetic field distribution at a given reciprocal lattice vector $\mathbf{q} = \mathbf{G}$. In the London model, which does not consider the vortex cores, $f(\mathbf{q}) = \phi_o/(1+\lambda^2 q^2)$, where λ is the London penetration depth (for UPt_3 at zero temperature λ = 6,000 Å). A much better solution can be obtained for a one-component superconductor by numerically solving the Ginzburg–Landau theory[24], and can be conveniently expressed as the product of the London model solution with a correction function $g(\mathbf{q}, B/B_{c2})$, where B_{c2} is the upper critical field. However, the observed form factor for UPt_3 decreases faster with temperature

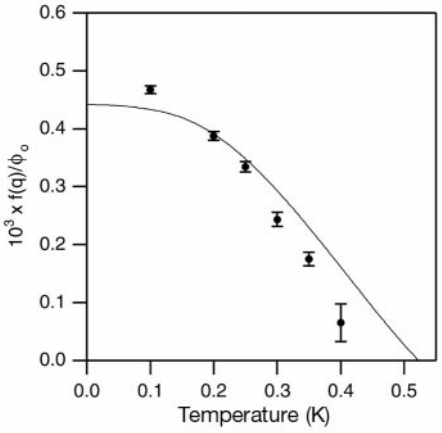

Figure 3 The measured temperature dependence of the form factor for the lowest-order diffraction process in an applied field of 0.19 T. At each temperature, the FLL was formed by the ZFC+FO process described in the text, and the diffracted intensity recorded without further changes in temperature or field. The line shows the calculated dependence of the form factor for a conventional BCS superconductor with the same parameters as our UPt_3 crystal ($dB_{c2}/dT = 7\,T\,K^{-1}$ at T_c = 550 mK and $\lambda(0)$ = 6,000 Å). The observed form factor decreases more rapidly than the BCS prediction as the B–A phase transition is approached. The error bars represent the statistical errors in the diffracted intensities.

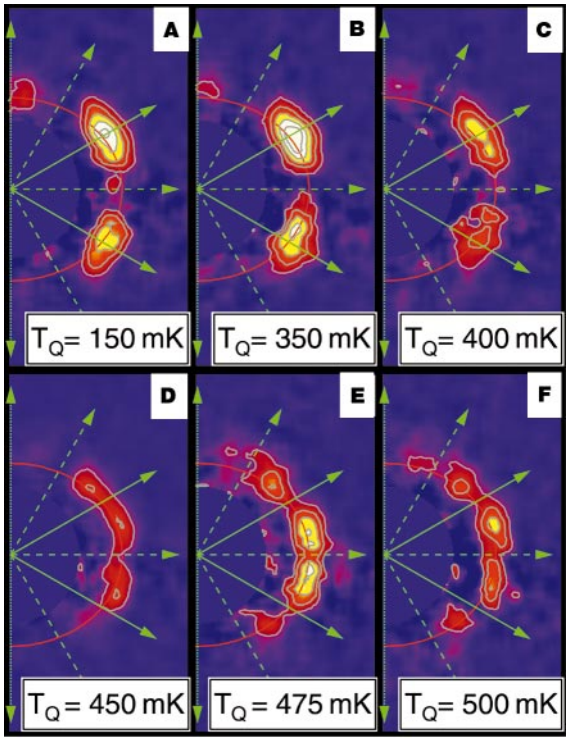

Figure 4 The transformation of the FLL orientation. The panels show the right-hand half of the detected images for diffraction from FLLs grown by the ZFC+FO procedure (see text) at various temperatures T_Q, and then quenched in constant field to low temperature (100–150 mK). The images show a transformation as the A phase is approached, from a single hexagonal lattice with nearest neighbours along **a*** at low temperature, to two new lattice orientations rotated by –15° and +15° from this direction. The contours and lines have the same meaning as in Fig. 2.

than predicted by this theory for a conventional temperature-evolution of one-component Ginzburg–Landau parameters (Fig. 3). This is principally due to the presence of additional nodes in the superconducting gap, which appear as the A phase is approached. The appearance of extra nodes is consistent with Saul's model[19] and also explains the observed increase in the magnetic penetration length seen in muon measurements[25,26]. Transverse ultrasound attenuation measurements[27] further show that the extra nodes lie parallel to the **c** axis. The resulting reduction in magnetic contrast, however, means that the FLL cannot be directly measured in the A phase in our experiment.

To study the A phase further, we grew FLLs at temperatures T_Q following the ZFC+FO procedure as above, but then subsequently cooled the lattices rapidly to low temperature in constant field. The quenched FLLs (Fig. 2D and Fig. 4) may now only be metastable, but they have an enhanced magnetic contrast characteristic of the lower temperature (100 mK) where the measurements were made. Following this procedure for $T_Q < 350$ mK, hexagonal lattices with the same geometry as found in the direct measurements were observed, with nearest-neighbour directions along the $\mathbf{a}^\star$ axes. But for $T_Q = 450$ mK, the image appears more rotationally disordered, but weakly aligned along new directions. Remarkably, for higher T_Q (475 mK $\leq T_Q <$ 520 mK), the observed FLLs were again extremely well ordered and clearly show this new alignment. By carefully measuring the spot positions, we conclude that for T_Q in this range the flux lines are still arranged in hexagonal lattices but with two equally populated nearest-neighbour orientations inclined at +15° and −15° to the crystal **a** axes.

As shown by Kogan[11], when $\kappa \gg 1$ ($\kappa = \lambda/\xi$, where ξ is the superconducting coherence length), the core energy of the vortices can be neglected, and the FLL symmetry can be calculated by extending the London model to include the lowest-order non-local corrections. The favoured FLL structure minimizes the free energy density, F, for a given flux density, where

$$F = \frac{B^2}{2\mu_0\phi_0}\sum_{\mathbf{q}=\mathbf{G}} f(\mathbf{q}) \qquad (2)$$

The sum extends over all reciprocal lattice vectors **G**, but is effectively cut off at $|\mathbf{q}| \approx 1/\xi$ by the vortex core correction to $f(\mathbf{q})$, which can be conveniently approximated[28] by $g(\mathbf{q}) = \exp(-\sqrt{2}q\xi)$ in the limit of $\kappa \gg 1$ ($\kappa \approx 60$ for UPt_3) and $B/B_{c2} \ll 1$. Non-local effects may additionally modify $f(\mathbf{q})$. To be more specific, we consider the angular dependence of the gap parameter in the A phase, projected into the basal plane, to be $\Delta(\mathbf{k}) \propto k_x k_y$ which is the lowest-order angular harmonic consistent with the E_{2u} model (k_x and k_y are direction cosines relative to the x and y axes). In the B phase, the second component of the order parameter is no longer zero and the basal plane gap anisotropy is smaller. This gives the following modified form for $f(\mathbf{q})$:

$$f(\mathbf{q}) = \frac{g(\mathbf{q})}{1 + \lambda^2\mathbf{q}^2 + c_1\lambda^4\mathbf{q}^4 + c_2\lambda^4\mathbf{q}_x^2\mathbf{q}_y^2} \qquad (3)$$

where c_1 is of the order of $1/\kappa^2$. c_2 measures the degree of the basal plane anisotropy of the superconductivity. It is expected to be very small at low temperature in the B phase, but increases with temperature as the B–A transition is approached, and attains a value of the order of $1/\kappa^2$ in the A phase, where the second component of the order parameter vanishes. For $c_2 = 0$, F is a minimum for an ideal hexagonal lattice with an arbitrary orientation. For small c_2 the deformation from the hexagonal structure remains small, but the free energy is now a minimum for two lattice orientations, inclined at +15° and −15° to the x-axis. Only for $c_2 \gg 1/\kappa^2$ does the lowest-energy configuration change to approach a square lattice.

Sixth-order powers of **q** must also be included in the denominator of equation (3) to account for the anisotropy of the Fermi surface. They are relevant only at low temperature in the B phase where the basal plane anisotropy of the superconducting gap becomes small. The crystal point group contains mirror planes along both **a** and $\mathbf{a}^\star$ directions, and so, considering the Fermi surface anisotropy alone, the free energy will have extrema when the FLL symmetry also respects these symmetries; the stable FLL is then hexagonal with nearest-neighbour directions along either **a** or $\mathbf{a}^\star$. It is not possible to deduce the precise anisotropy of the Fermi velocity from existing measurements of the Fermi surface, although available data[29] show that for the dominant sheets the projected surface areas are larger, and the electronic effective masses smaller, parallel to **a** directions. Both effects act in the same sense to suggest that the Fermi velocity, and therefore the screening currents, are larger parallel to **a**. The FLL nearest neighbours would therefore be expected to lie along $\mathbf{a}^\star$, as was observed for $T_Q < 350$ mK. In the theoretical description[19] of the unconventional superconductivity of UPt_3, the orientation of the order parameter and therefore of the superconducting gap is determined by the coupling of the superconductivity to a weak symmetry-breaking field. In zero magnetic field this mechanism is responsible for separating the two superconducting transition temperatures which would otherwise be degenerate. The symmetry-breaking field is usually attributed to an observed quasi-static antiferromagnetic order[30] with the ordered moments and ordering vectors lying along $\mathbf{a}^\star$ directions[31]. In the E_{2u} model, this fixes the azimuthal orientations of the antinodes in the superconducting gap to either (1) coincide with **a** and $\mathbf{a}^\star$ directions, or (2) bisect adjacent **a** and $\mathbf{a}^\star$ directions; one choice occurs in the C phase, while the other is realised in the A phase (Fig. 1). From our experiment we can conclude it is the second choice that occurs in the A phase. In most other theoretical models with different candidate symmetry scenarios, such as the E_{1g} model[32], the gap antinodes always lie along **a** and $\mathbf{a}^\star$ directions and they cannot therefore explain the unusual FLL orientation we observe. It is important also to stress that our result is independent of any domain structure of the symmetry-breaking field. Different domains will be related by rotations through multiples of 60°, but give rise to the same hexagonal FLL. □

Received 29 November 1999; accepted 10 May 2000.

1. Abrikosov, A. A. On the magnetic properties of superconductors of the second group. *JETP* **32,** 1442–1452 (1957).
2. Kleiner, W. H., Roth, L. M. & Autler, S. H. Bulk solution of Ginzburg-Landau equations for type II superconductors: upper critical field region. *Phys. Rev.* **133,** A1226–A1227 (1964).
3. M°K. Paul, D. *et al.* Nonlocal effects and vortex lattice transitions in YNi_2B_2C. *Phys. Rev. Lett.* **80,** 1517–1520 (1998).
4. Takanaka, K. Correlation between the flux-line lattice and crystal axis in a mixed state of superconductors. *Prog. Theor. Phys.* **50,** 365–369 (1973).
5. Heffner, R. H. & Norman, M. R. Heavy fermion superconductivity. *Comments Condens. Matter Phys.* **17,** 361–408 (1996).
6. Leggett, A. J. in *Electron: A Centenary Volume* (ed. Springford, M.) 148–181 (Cambridge Univ. Press, Cambridge, 1999).
7. Eskildsen, M. R. *et al.* Intertwined symmetry of the magnetic modulation and the flux-line lattice in the superconducting state of $TmNi_2B_2C$. *Nature* **393,** 242–245 (1998).
8. Kleiman, R. N. *et al.* Neutron diffraction from the vortex lattice in the heavy-fermion superconductor UPt_3. *Phys. Rev. Lett.* **69,** 3120–3123 (1992).
9. Yaron, U. *et al.* Small angle neutron scattering of the vortex lattice in the UPt_3 mixed state: direct structural evidence for the B→C transition. *Phys. Rev. Lett.* **78,** 3185–3188 (1997).
10. Joynt, R. Theory of neutron diffraction from the vortex lattice in UPt_3. *Phys. Rev. Lett.* **78,** 3189–3192 (1997).
11. Kogan, V. G. *et al.* Nonlocal electrodynamics and low temperature magnetisation of clean high κ superconductors. *Phys. Rev. B* **54,** 12386–12396 (1996).
12. Kogan, V. G. *et al.* Vortex lattice transitions in borocarbides. *Phys. Rev. B* **55,** R8693–R8696 (1997).
13. Riseman, T. M. *et al.* Observation of a square flux-line lattice in the unconventional superconductor Sr_2RuO_4. *Nature* **396,** 242–245 (1998).
14. Brison, J. P. *et al.* Magnetism and superconductivity in heavy fermion systems. *J. Low Temp. Phys.* **95,** 145–152 (1994).
15. Kycia, J. B. *et al.* Suppression of superconductivity in UPt_3 single crystals. *Phys. Rev. B* **58,** R603–R606 (1998).
16. Adenwalla, S. *et al.* Phase diagram of UPt_3 from ultrasonic velocity measurements. *Phys. Rev. Lett.* **65,** 2298–2301 (1990).
17. Gorkov, L. P. Superconductivity in heavy fermion systems. *Sov. Sci. Rev. A Phys.* **9,** 1–116 (1987).
18. Mineev, V. P. & Samokhin, K. V. *Introduction to Unconventional Superconductivity* (Gordon & Breach Science, Amsterdam, 1999).
19. Sauls, J. A. The order parameter in the superconducting phases of UPt_3. *Adv. Phys.* **43,** 113–141 (1994).

20. London, F. *Superfluids* (Wiley, New York, 1950).
21. Tokuyasu, T. A., Hess, D. W. & Sauls, J. A. Vortex states in an unconventional superconductor and the mixed states of UPt_3. *Phys. Rev. B* **41,** 8891–8903 (1990).
22. Luk'yanchuk, I. A. & Zhitomirsky, M. E. Magnetic properties of unconventional superconductors. *Supercond. Rev.* **1,** 207–256 (1995).
23. Yaron, P. L. *et al.* Neutron diffraction studies of flowing and pinned magnetic flux lattices in 2H-$NbSe_2$. *Phys. Rev. Lett.* **73,** 2748–2751 (1994).
24. Brandt, E. H. Precision Ginzburg-Landau solution of ideal vortex lattices for any induction and symmetry. *Phys. Rev. Lett.* **78,** 2208–2211 (1997).
25. Broholm, C. *et al.* Anisotropic temperature dependence of the magnetic-field penetration in superconducting UPt_3. *Phys. Rev. Lett.* **65,** 2062–2065 (1990).
26. Yaouanc, A. *et al.* Strong axial anisotropy of the magnetic penetration length in superconducting UPt_3. *J. Phys. Condens. Matter* **10,** 9791–9798 (1998).
27. Ellman, B., Taillefer, L. & Poirier, M. Transverse ultrasound revisited: a directional probe of the A phase in UPt_3. *Phys. Rev. B* **54,** 9043–9046 (1996).
28. Clem, J. R. Simple model for the vortex core in a type II superconductor. *J. Low Temp. Phys.* **18,** 427–434 (1974).
29. Taillefer, L. & Lonzarich, G. G. Heavy fermion quasi-particles in UPt_3. *Phys. Rev.Lett.* **60,** 1570–1573 (1988).
30. Hayden, S. M., Taillefer, L., Vettier, C. & Flouquet, J. Antiferromagnetic order in UPt_3 under pressure: Evidence for a direct coupling to superconductivity. *Phys. Rev. B* **46,** 8675–8678 (1992).
31. Aeppli, G. *et al.* Magnetic order and fluctuations in superconducting UPt_3. *Phys. Rev. Lett.* **60,** 615–618 (1988).
32. Park, K. A. & Joynt, R. Phase diagram of UPt_3 in the E_{1g} model. *Phys. Rev. Lett.* **74,** 4734–4737 (1995).

Correspondence and requests for materials should be addressed to A.H. (e-mail: huxley@drfmc.ceng.cea.fr).

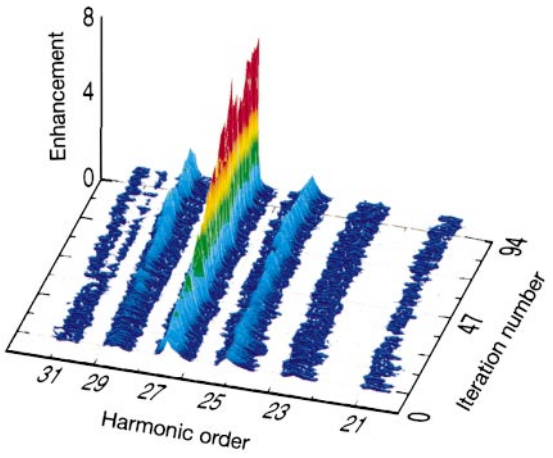

Figure 1 Optimization of a single (27th) harmonic in argon while suppressing adjacent harmonics. The optimization criterion (fitness function) for this run corresponded to $f = \Sigma s_i - \Sigma s_j - \Sigma s_k$, where s corresponds to the signal level of a CCD pixel, and the ranges i, j and k represent the pixels corresponding to a 0.5-nm spectral bandwidth centred around the 25th, 27th and 29th harmonic. The peak enhancement for the 27th harmonic is a factor of 8, while the energy enhancement is a factor of 4.6. The contrast ratio between the 27th harmonic and adjacent harmonic increases by a factor of 4.

Shaped-pulse optimization of coherent emission of high-harmonic soft X-rays

R. Bartels*, S. Backus*, E. Zeek*, L. Misoguti*, G. Vdovin†, I. P. Christov‡, M. M. Murnane* & H. C. Kapteyn*

* *JILA and Department of Physics, University of Colorado and National Institute of Standards and Technology, Campus Box 440, Boulder, Colorado 80309-0440, USA*
† *Delft University of Technology, 2600 GA Delft, The Netherlands*
‡ *Department of Physics, Sofia University, Sofia, Bulgaria*

When an intense laser pulse is focused into a gas, the light–atom interaction that occurs as atoms are ionized results in an extremely nonlinear optical process[1–3]—the generation of high harmonics of the driving laser frequency. Harmonics that extend up to orders of about 300 have been reported[4,5], some corresponding to photon energies in excess of 500 eV. Because this technique is simple to implement and generates coherent, laser-like, soft X-ray beams, it is currently being developed for applications in science and technology; these include probing the dynamics in chemical and materials systems[6] and imaging[7]. Here we report that by carefully tailoring the shape[8] of intense light pulses, we can control[9,10] the interaction of light with an atom during ionization, improving the efficiency of X-ray generation by an order of magnitude. We demonstrate that it is possible to tune the spectral characteristics of the emitted radiation, and to steer the interaction between different orders of nonlinear processes.

This work builds on a number of other recent advances in laser and nonlinear-optical science and technology. The use of temporally shaped ultrashort pulses to create 'designer' atomic wavepackets[11], to control two-photon absorption[12,13], and to control molecular processes[11,14] has been a topic of increasing interest as laser technology has developed. Recent work has demonstrated techniques to increase the conversion efficiency of high-harmonic generation by using waveguide[15] and new focusing geometries[16,17], and very short duration (≤25 fs, or ~10 optical cycles) light pulses[18]. It has also been shown that the temporal ordering of colours in the light pulse affects the spectral characteristics of the high-harmonic radiation[19,20]. However, that work was limited to simple adjustment of the light pulse 'chirp' and did not reveal any ability to selectively control the high harmonic generation (HHG) process or to improve overall conversion efficiency.

The present work uses a newly developed laser system that generates high-power ultrafast laser pulses with the capability of temporally reshaping them in a very precise and flexible manner[21]. We show that very subtle changes (resulting in changes in the time duration of the light pulse of only a few femtoseconds) can manipulate the electronic response of an atom, and thereby control the spectral characteristics and brightness of the soft X-ray coherent radiation. We have found this effect to be very general, occurring over a wide range of parameters and in different gases. In light of past work, the effectiveness of this technique is unexpected. It illustrates significant differences between low-order nonlinear processes such as second-harmonic generation and high-order processes such as HHG that are inherently non-perturbative. Furthermore, under some conditions it is possible to channel most of the high-harmonic emission into a single spectral peak creating a coherent, nearly monochromatic soft X-ray source with a greatly enhanced brightness.

In our experiment, we focus light pulses from an ultrafast laser system with a repetition rate of 1 kHz and a pulse energy of up to 1 mJ into a 175-μm diameter, gas-filled capillary waveguide. The pulse peak intensity ($\sim 2 \times 10^{14}$ W cm^{-2}) is sufficient to field-ionize the atoms (typically argon), in the process generating high-harmonic extreme ultraviolet (XUV) radiation. The capillary waveguide allows us to create an extended region of high laser intensity and long coherence length to efficiently generate the high-harmonic radiation[15], which is observed using an X-ray charge-coupled device (CCD) camera directly coupled to a grazing-incidence spectrometer.

The laser system incorporates a micromachined deformable mirror pulse-shaping apparatus[22]. This adaptive optic element is used in a position within the laser system where the frequency components of the light pulse are spatially separated and can change the relative path length of the various colours, thus reordering the arrival times of the colours of the short pulse. The light pulse bandwidth is about 80 nm full-width at half-maximum (FWHM) centred at 800 nm, and is not altered by the pulse shaper.